Martensitic Transformations and Mechanical and Corrosion Properties of Fe-Mn-Si Alloys for Biodegradable Medical Implants

RICHARD DREVET, YULIA ZHUKOVA, POLINA MALIKOVA, SERGEY DUBINSKIY, ANDREY KOROTITSKIY, YURY PUSTOV, and SERGEY PROKOSHKIN

The Fe-Mn-Si alloys are promising materials for biodegradable metallic implants for temporary healing process in the human body. In this study, three different compositions are considered (Fe23Mn5Si, Fe26Mn5Si, and Fe30Mn5Si, all in wt pct). The phase composition analysis by XRD reveals ε-martensite, α-martensite, and γ-austenite in various proportions depending on the manganese amount. The DSC study shows that the starting temperature of the martensitic transformation (M_s) of the alloys decreases when the manganese content increases (416 K, 401 K, and 323 K (143 °C, 128 °C, and 50 °C) for the Fe23Mn5Si, Fe26Mn5Si, and Fe30Mn5Si alloys, respectively). Moreover, mechanical compression tests indicate that these alloys have a much lower Young's modulus (E) than pure iron (220 GPa), *i.e.*, 145, 133, and 118 GPa for the Fe23Mn5Si, Fe26Mn5Si, and Fe30Mn5Si alloys, respectively. The corrosion behavior of the alloys is studied in Hank's solution at 310 K (37 °C) using electrochemical experiments and weight loss measurements. The corrosion kinetics of the Fe-Mn-Si increases with the manganese content (0.48, 0.59, and 0.80 mm/year for the Fe23Mn5Si, Fe26Mn5Si, and Fe30Mn5Si alloys, respectively). The alloy with the highest manganese content shows the most promising properties for biomedical applications as a biodegradable and biomechanically compatible implant material.

https://doi.org/10.1007/s11661-017-4458-2

I. INTRODUCTION

RECENTLY, the biodegradable metallic implants for temporary applications have attracted a lot of attention in biomedical science. Their degradation properties in a corrosive environment are used to avoid repeated surgical intervention for the implant removal after the completion of the healing process.[1–6] Among the biodegradable metallic materials, the Fe-Mn-Si alloys, initially considered only as shape memory and damping alloys,[7,8] are the most promising ones. Indeed, they degrade inside the human body faster than pure iron known to have a rather low degradation rate,[9–12] while they degrade slower than magnesium alloys known to have a too high degradation rate.[13,14] Additionally, it is noteworthy that manganese and silicon are nontoxic elements for the human body since they are well established to be essential for the body function of all mammals.[6,15] Several previous studies have shown that the mechanical properties of the Fe-Mn-Si alloys are appropriate and close to those of stainless steels with manganese content between 23 and 30 wt pct.[16–18] Another important factor for the implant use of Fe-Mn-Si alloys is their biomechanical compatibility. Indeed, the mechanical properties of a bone implant used for load-bearing applications have to be close to those of the surrounding bone tissues.[2] Otherwise, the mechanical mismatch leads to stress-shielding effect that promotes the resorption of bone tissues due to the lack of appropriate stress naturally required for bone growth.[19] This requirement can be met by decreasing the Young's modulus of the metallic material as much as possible. As for the Fe-Mn-Si biodegradable alloys, this property is overlooked, whereas the development of the reversible $\gamma \leftrightarrow \varepsilon$ martensitic transformation makes it possible to obtain a low Young's modulus in the case when their M_s temperature is close to the body temperature due to a pre-transformation lattice softening phenomenon.[8,20,21] This advantage is of great importance for human body

RICHARD DREVET, YULIA ZHUKOVA, POLINA MALIKOVA, SERGEY DUBINSKIY, ANDREY KOROTITSKIY, YURY PUSTOV and SERGEY PROKOSHKIN are with the National University of Science and Technology "MISiS", Leninskiy prosp. 4, Moscow 119049, Russian Federation. Contact e-mail: richarddrevet@misis.ru
Manuscript submitted April 19, 2017.
Article published online January 3, 2018

implants.[22] Furthermore, due to their shape memory and superelastic properties, such alloys could also be envisaged for specific coronary stent applications if the temperature range of the reverse martensitic transformation is below the human body temperature.[11–14]

Although several Fe-Mn-Si alloy compositions can be considered as promising, few studies report on the impact of the manganese content on their biodegradation ability in physiological environment. Also, their Young's modulus value is not well documented. This study presents three Fe-Mn-Si alloys containing different manganese amounts and the impact of the manganese content on their degradation in a physiological solution that mimics the body fluids, as well as mechanical properties, especially the Young's modulus. For the purpose of this research, the synthesized alloys are characterized by X-ray diffraction (XRD), differential scanning calorimetry (DSC), and mechanical compression testing in order to evaluate the Young's modulus value. Besides, the corrosion and electrochemical behavior in the physiological solution of the three alloys is assessed by electrochemical techniques, *i.e.*, the open circuit potential and polarization measurements. For comparison, the corrosion rate of the alloys is also determined from weight loss measurements carried out after the immersion studies.

II. EXPERIMENTAL PROCEDURES

A. *Synthesis and Physical Characterization*

The starting materials used to synthesize the alloys are Armco® commercially pure iron (99.85 pct), manganese (99 pct), and silicon (99 pct). The three studied manganese amounts in the alloys are 23, 26, and 30 wt pct, whereas the silicon content is fixed at 5 wt pct. The studied alloys are labeled as Fe23Mn5Si, Fe26Mn5Si, and Fe30Mn5Si, respectively. The alloy ingots are obtained by a vacuum arc remelting process with a nonconsumable tungsten electrode that is conventionally used to obtain ingots with a low impurity level. Then the synthesized alloys are homogenized by annealing in the air inside an electrical furnace at 1173 K (900 °C) for 60 minutes and water-quenched. Their microstructure is observed by optical microscopy (*Carl Zeiss Jena*) using the samples prepared by mechanical cutting, polishing with 320- to 1200-grit emery papers followed by chemical etching in 5 pct HNO_3 ethanol solution, ensuring the complete removal of the damaged and oxidized surface layer. The chemical homogeneity of the synthesized alloys is assessed by X-ray maps obtained from a scanning electron microscope (SEM, JEOL JSM 6480LV) equipped with an energy-dispersive spectrometer (EDS, JED-2300F).

The crystalline phase composition of the alloys is studied by X-ray diffraction (XRD) with a *DRON-3* diffractometer using $Cu_{K\alpha}$ radiation ($\lambda = 0.154178$ nm). The X-ray diffractograms are recorded in 20 to 80 deg 2θ angle range with a step of 0.1 deg. The crystal structures of the phases are identified from the diffraction files provided by the International Centre for Diffraction Data (ICDD).

The yield stress $\sigma_{0.2}$ and the apparent Young's modulus E of the synthesized alloys are determined from the stress–strain curves obtained during compression tests with a *Gleeble System 3800* (*DSI, USA*) equipped with the *Hydrawedge-II* module. This mechanical characterization requires samples of 4 mm diameter × 6 mm height. The compression strain rate is $0.002\ s^{-1}$. The Young's modulus is determined from the unloading part of the compression curve in the range from ~ 0.5 to 2 pct strain. A statistical analysis of the mechanical properties of the alloys is based on nine to ten measurements of E and three measurements of $\sigma_{0.2}$ for each alloy. The analysis includes determining the standard deviations and confidence error limits using a standard procedure as follows: (1) calculation of a standard deviation of an averaged value X as $s_X = s_{xi}/\sqrt{n}$, where s_{xi} is the standard deviation of i-th count x_i, and (2) calculation of a confidence interval of X as $\delta_X = \pm t_{P,f}\, s_X/\sqrt{n}$, where $t_{P,f}$ is the tabulated value of the Student's coefficient, $P = 0.95$ is the confidence probability, and $f = n - 1$.

The martensitic transformation temperatures are measured with differential scanning calorimetry (DSC) performed with a *PerkinElmer* calorimeter (*DSC 4000*) by heating the samples (5 mm in diameter × 3 mm in height) from room temperature to 573 K (300 °C) and then cooling to 213 K (− 60 °C) with a heating–cooling rate of 10 K per minute. This procedure is consecutively repeated twice.

B. *Assessment of Corrosion Properties*

The corrosion properties of the three synthesized Fe-Mn-Si alloys are assessed from electrochemical measurements and compared to those of pure iron and binary Fe-Mn alloy. Thin plates of 10 × 10 mm are cut in the ingots and then immersed in Hank's solution at 310 K (37 °C), which simulates the body fluids according to the concentration of the dissolved salts in 1 liter of distilled water: 8 g NaCl, 0.4 g KCl, 0.12 g $Na_2HPO_4{\cdot}12H_2O$, 0.06 g KH_2PO_4, 0.2 g $MgSO_4{\cdot}7H_2O$, 0.35 g $NaHCO_3$, and 0.14 g $CaCl_2$. In these conditions, the pH value of the solution is 7.4. The electrochemical studies are carried out with an IPC-Pro electronic potentiostat (*Volta Co*). The obtained data are studied with commercial software *IPC2000*. The reference electrode is a saturated silver chloride electrode (SSCE), and the auxiliary electrode is a platinum electrode. For the polarization curves, the potential is measured with a scan rate of 0.2 mV/s. The polarization experiments are performed in triplicate. From the Tafel representation of the polarization curves, the corrosion current density ($i_{corr.}$) is extracted to determine the corrosion rate (K_r) of the alloys as follows[23]:

$$K_r = \frac{i_{corr.} \times A \times 10^4}{n \times F \times \rho}, \qquad [1]$$

where A is the atomic mass of the alloy, n is the number of the transferred electrons according to the corrosion reaction, and F is the Faraday constant ($F = 96{,}500$ C/mol).

For comparison, the corrosion rate ($K_{\Delta m}$) is also determined from weight loss measurements according to the following equation[23]:

$$K_{\Delta m} = \frac{8.76 \times (m_0 - m_\tau)}{\rho \times S \times \tau}, \quad [2]$$

where m_0 and m_τ (kg) are the initial and the final mass of the alloy, respectively, S is the corroded surface of the alloy ($S = 2.4 \times 10^{-4}$ m^2), τ (s) is the time duration of the corrosion experiment, and ρ is the density of the alloy ($\rho_{Fe23Mn5Si} = 6.92 \times 10^3$ kg/m^3, $\rho_{Fe26Mn5Si} = 6.91 \times 10^3$ kg/m^3, $\rho_{Fe30Mn5Si} = 6.89 \times 10^3$ kg/m^3).

III. RESULTS AND DISCUSSION

A. *Synthesis and Structural and Mechanical Characterization of the Fe-Mn-Si Alloys*

The optical micrograph in Figure 1(a) indicates that the microstructure of the as-cast Fe30Mn5Si alloy (without any homogenization heat treatment) is composed of dendrites.

According to the literature about the Fe-Mn alloys, the annealing homogenization was first conducted at 1123 K (850 °C) for 60 minutes.[16] However, the corresponding microstructural observation of the Fe30Mn5Si alloy reveals that the initial dendritic morphology is not significantly modified (see Figures 1(a) and (b)). When the heat treatment is carried out at 1173 K (900 °C) for 60 minutes, the microstructural observation is changed, evidencing austenite grains of several hundred micrometers in diameter with martensite plates in the grain interior (see Figure 1(c)). Therefore, the three synthesized alloys (Fe23Mn5Si, Fe26Mn5Si, and Fe30Mn5Si) are water-quenched after heating at 1173 K (900 °C) for 60 minutes. The microstructure of the Fe23Mn5Si and Fe26Mn5Si alloys is composed of the same phase constituents, as well (Figures 1(d) and (e)).

The chemical homogeneity of the synthesized alloys after the annealing treatment followed by water quenching is observed in the X-ray maps obtained by EDS (Figure 2).

They show a homogeneous distribution of iron, manganese, and silicon in each alloy. The elemental concentration remains constant in the large studied area. Note that no reliable impurity levels can be detected in the samples by the EDS method.

The phase compositions of the quenched alloys are characterized by the X-ray diffraction method with a

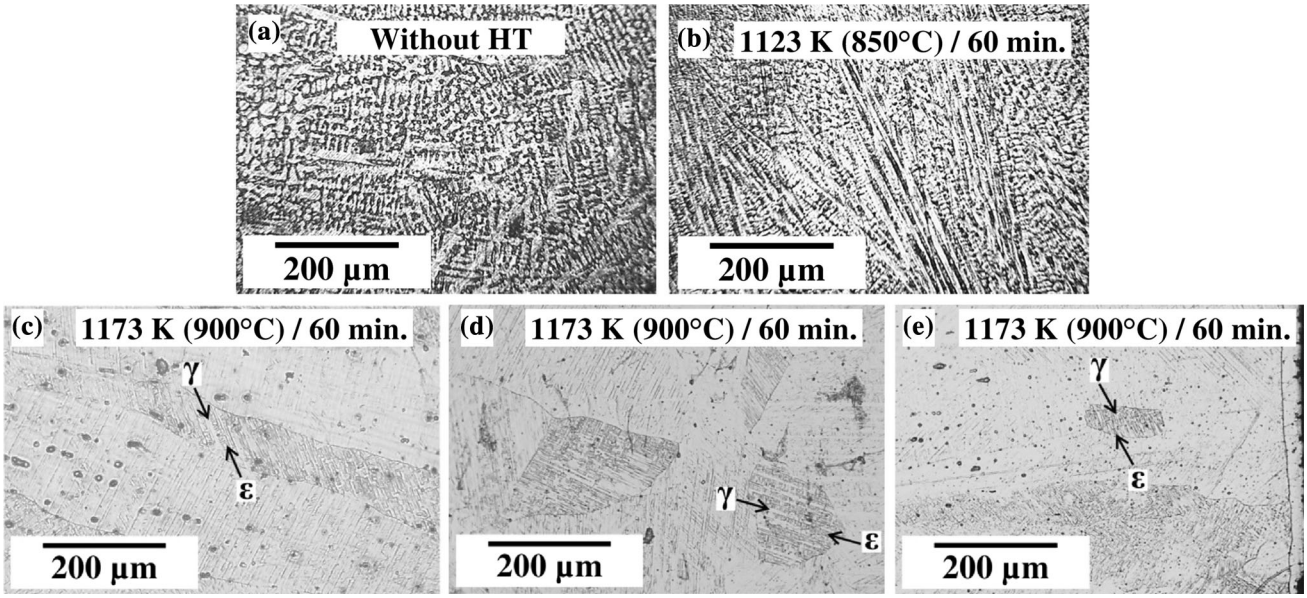

Fig. 1—Microstructure of (*a*) Fe30Mn5Si as-cast, (*b*) Fe30Mn5Si after 1123 K (850 °C) / 60 min, (*c*) Fe30Mn5Si after 1173 K (900 °C)/60 min, (*d*) Fe23Mn5Si after 1173 K (900 °C)/60 min, and (*e*) Fe26Mn5Si after 1173 K (900 °C)/60 min.

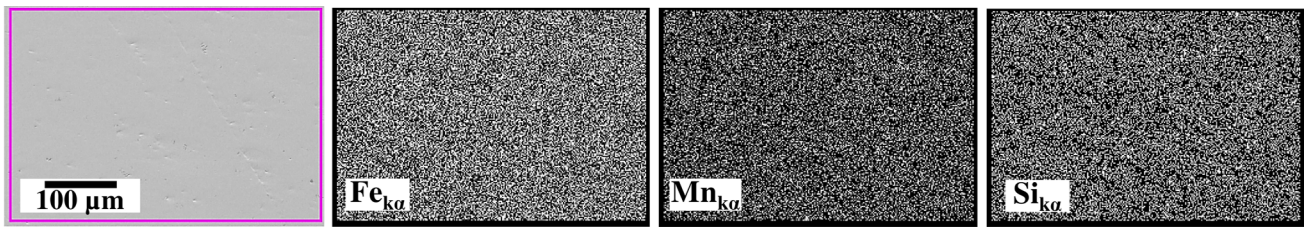

Fig. 2—X-ray maps of the Fe30Mn5Si alloy.

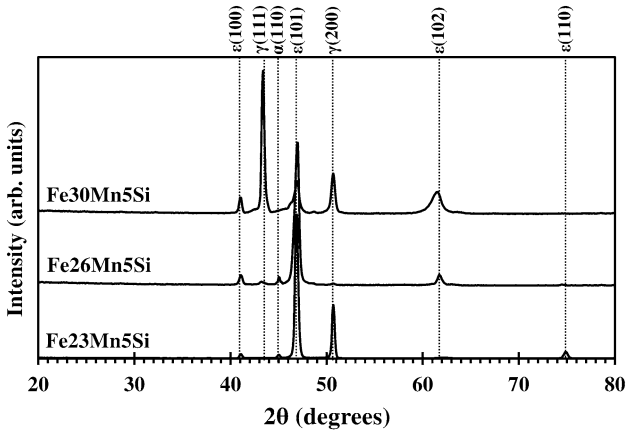

Fig. 3—X-ray diffraction patterns of the synthesized Fe-Mn-Si alloys.

higher precision (Figure 3). The XRD patterns of the three alloys are different. The diffractogram of the Fe23Mn5Si alloy reveals a mixture of three phases: HCP ε-martensite, BCC α-martensite accompanied with retained FCC γ-austenite. In the case of the Fe26Mn5Si alloy, mainly two phases are observed: ε-martensite and a low amount of α-martensite. Very low amounts of γ-austenite and β-manganese are also present; however, their X-ray lines are not visible at the intensity scale used in Figure 3. On the other hand, the XRD pattern of the Fe30Mn5Si alloy also indicates only two phases: γ-austenite as the major one and ε-martensite. Note that it was experimentally observed that the Mn content between 13 and 22 wt pct in the Fe-Mn binary alloys promotes the presence of the ε-martensite phase, whereas the Mn content higher than 22 wt pct promotes the presence of the γ-austenite phase.[24] However, in the case of the Fe-Mn-Si alloys, this observation is not as much pronounced as expected due to the presence of 5 wt pct silicon in the alloy. These observations highlight that the martensitic transformation $\gamma \rightarrow \varepsilon$ is much more advanced in the case of the Fe26Mn5Si and Fe23Mn5Si alloys as compared to the Fe30Mn5Si alloy. As described by Gavriljuk *et al.*,[25] the silicon lowers stacking fault energy of the austenite in the Fe-Mn-Si alloys, which favors the ε-martensite formation.

This information can be correlated with the DSC curves in Figure 4, which proves the martensitic transformations during the cooling process.

In the case of the Fe23Mn5Si alloy, the exothermal $\gamma \rightarrow \varepsilon$ transformation followed by the $\varepsilon \rightarrow \alpha$ transformation is clearly observable, which justifies the high quantity of the martensitic phases highlighted from the XRD results (Figure 3). The corresponding starting temperature is well defined at M_s = 416 K (143 °C). The similar transformation sequence is observable from the DSC cooling curve of the Fe26Mn5Si alloy for which the ε- and α-martensites are the main phases identified from the XRD results. The corresponding M_s temperature is well defined at 401 K (128 °C). These results contrast with those obtained for the Fe30Mn5Si alloy. In the latter case, the phase transformation occurs in an extended

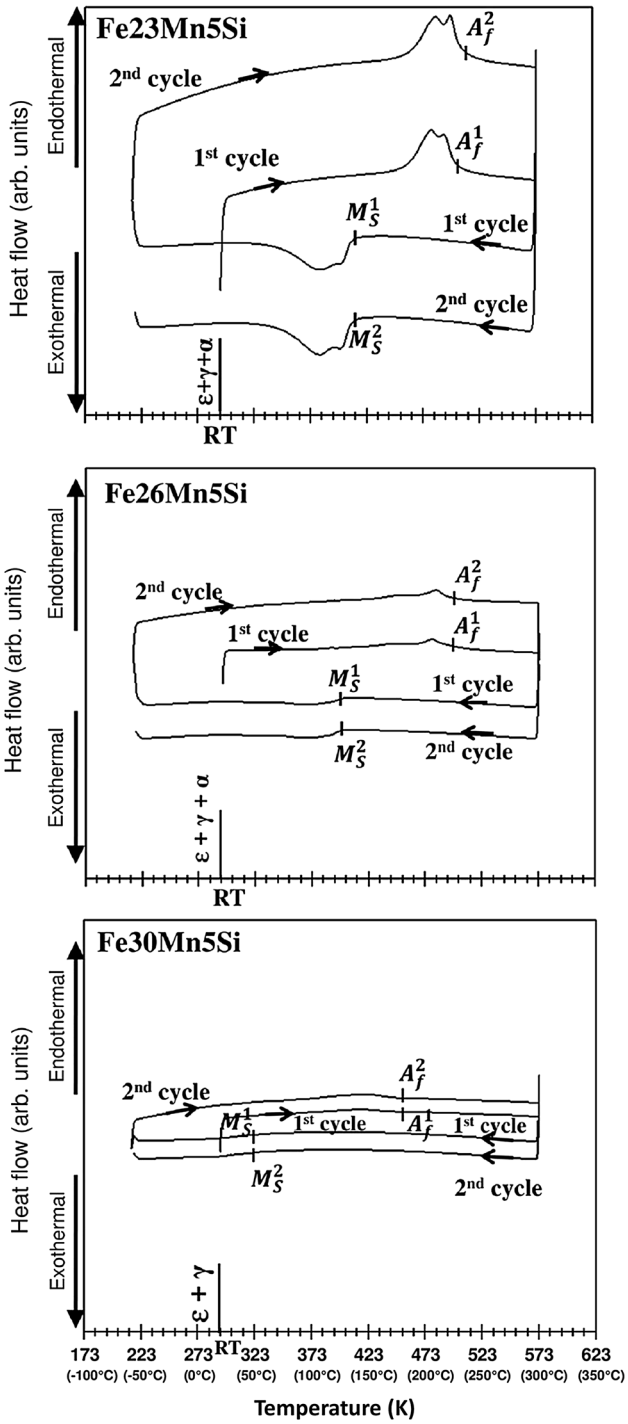

Fig. 4—DSC curves of the synthesized Fe-Mn-Si alloys obtained during two heating/cooling cycles.

temperature range, and the exothermal peak is much less pronounced. The corresponding M_s temperature is significantly lowered down to 323 K (50 °C), and the transformation continues during the cooling step beyond the measuring limit of 213 K (− 60 °C). This modification could be linked to the crystal lattice strain due to higher manganese content in the alloy.[24] Indeed, the corresponding XRD pattern in Figure 3

points out a more retained γ-austenite phase indicating that the martensitic transformations ($\gamma \rightarrow \varepsilon$ and so $\varepsilon \rightarrow \alpha$) are less advanced. Nevertheless, even if the kinetics of the transformation reaction is slowed by the increase of the manganese amount in the alloy, it is worth noting the promising decrease of the martensitic transformation temperature in the case of the Fe30Mn5Si alloy. First, such alloys could be expected to be used inside the human body as implant materials with the shape memory properties. For this purpose, the martensitic transformation temperature has to be further lowered below the body temperature.[2,5] This objective could be reached with an appropriate thermomechanical treatment able to modify the microstructure or the grain size of the alloy and/or by the addition of appropriate alloying elements.[26,27]

The most important result at the alloy characterization stage of the present study is obtained by compression mechanical tests (Figure 5).

The Young's modulus values of the synthesized alloys determined from the unloading branch of the stress–strain curve are 145, 133, and 118 GPa for the Fe23Mn5Si, Fe26Mn5Si, and Fe30Mn5Si alloys, respectively (Table I). These values are obviously much lower than that of a commercially pure iron (226 GPa) and comparable with that of commercially pure titanium (about 110 GPa), which is the most widespread implant material. In addition, it is noticeable that an increase of the manganese amount in the alloy decreases its Young's modulus. This property is really essential for bone implant applications, for which low Young's modulus values are required to avoid mechanical mismatches between the bone tissues and the metal implant. This parameter is a crucial factor for transferring the most appropriate mechanical stress to the surrounding bone.[28] Particularly, for the load-bearing applications, this mechanical mismatch leads to stress shielding that reduces the bone density (osteopenia) according to the Wolff's law.[29] This phenomenon corresponds to a structural adaptation of the bone tissues to the mechanical loads to which they are subjected. Thus, the biomechanical compatibility of the studied alloys is much higher than that of the commercially pure iron and comparable with that of the commercially pure titanium. Note that the yield stress $\sigma_{0.2}$ values of the Fe-Mn-Si alloys (198, 211, and 171 MPa for the Fe23Mn5Si, Fe26Mn5Si, and Fe30Mn5Si, respectively) are close to those of the most high-strength cortical bone tissues measured in the longitudinal direction (~ 205 MPa) and higher than the values measured in the transverse direction (~ 131 MPa), which ensures mechanical reliability of implants during their lifetime.[30]

Comparing the mechanical properties measured for the three synthesized materials, the Fe30Mn5Si alloy appears to be the most suitable for bone implant applications in terms of biomechanical compatibility. A further increase in the Mn content does not seem reasonable due to suppression of the martensitic

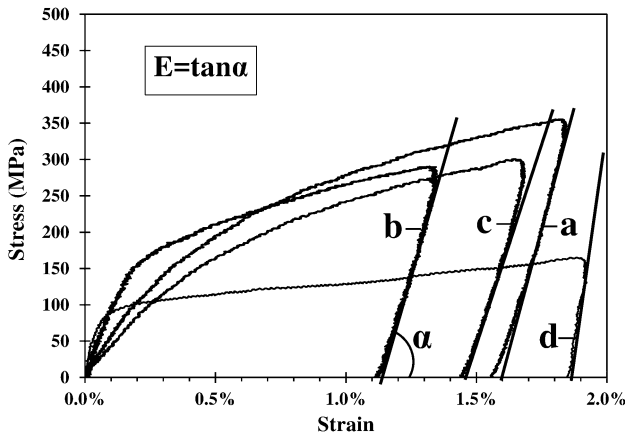

Fig. 5—Compressive stress–strain curves of (*a*) Fe23Mn5Si, (*b*) Fe26Mn5Si, and (*c*) Fe30Mn5Si alloys and (*d*) commercially pure iron.

Table I. Young's Modulus (E) and Yield Stress ($\sigma_{0.2}$) of the Synthesized Alloys

	E (GPa)	$\sigma_{0.2}$ (MPa)
Fe23Mn5Si	145 ± 10	198 ± 18
Fe26Mn5Si	133 ± 16	211 ± 21
Fe30Mn5Si	118 ± 4	171 ± 15

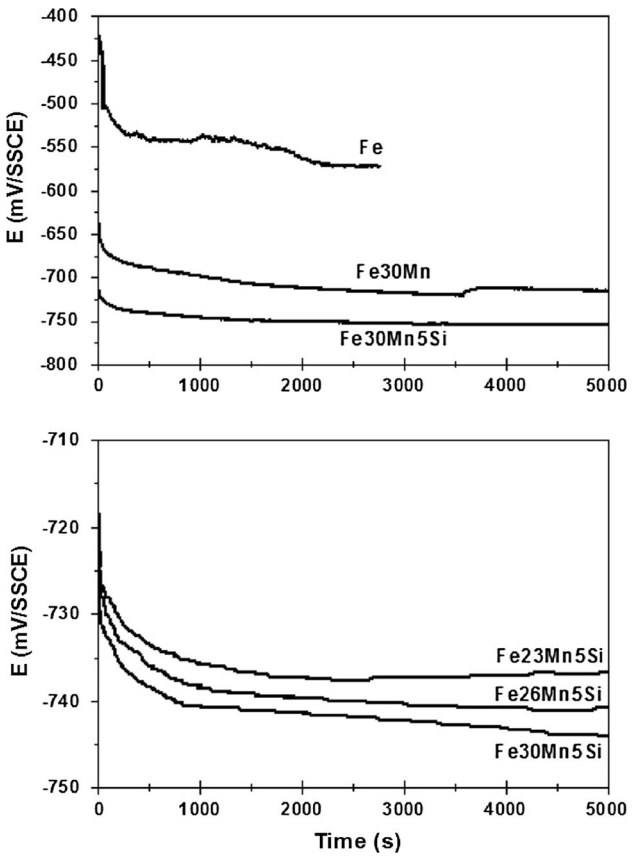

Fig. 6—Open circuit potential measurements of the synthesized Fe-Mn-Si alloys immersed in the physiological solution at 310 K (37 °C) (comparison with Fe and Fe-Mn).

transformation (as supported by the DSC results) leading to the absence of the shape memory effect. In general, Fe30Mn5Si alloy can be considered as an optimal shape memory alloy in the Fe-Mn-Si system. Nevertheless, the detailed characterization of the shape memory, superelasticity, and/or low Young's modulus phenomenon should be the issue of further investigation. Moreover, further control of the shape memory behavior and further improvement in the mechanical properties of the Fe30Mn5Si alloy can be expected by appropriate thermomechanical treatments (*e.g.*, rolling, annealing) with the objective to modify the microstructure, the texture, and/or the grain size of the alloy.[31,32] Alternatively, the addition of some amount of chemical elements, such as palladium or cobalt, to the alloy can be also considered to improve these properties.[33,34]

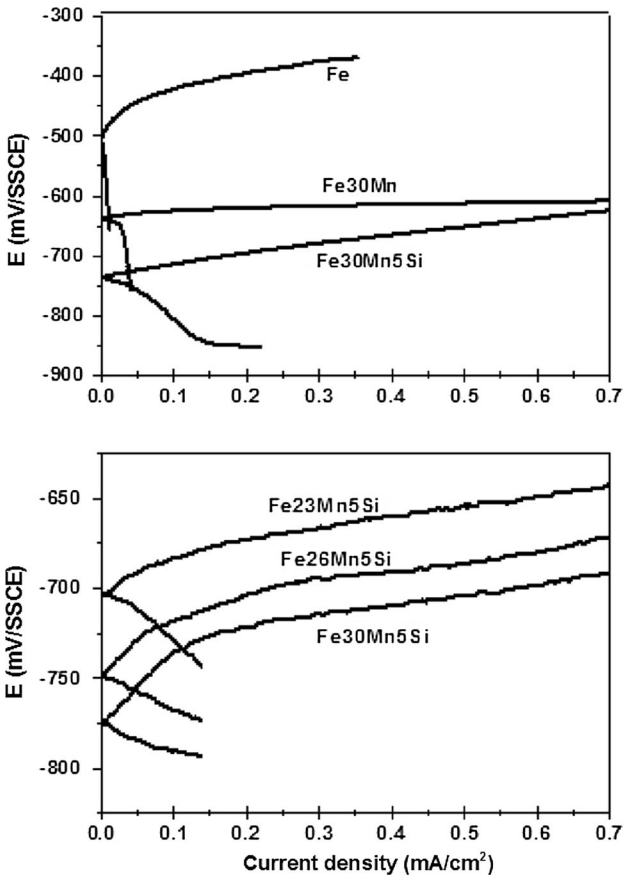

Fig. 7—Polarization curves of the synthesized Fe-Mn-Si alloys immersed in the physiological solution at 310 K (37 °C) (comparison with Fe and Fe-Mn).

B. *Corrosion and Electrochemical Properties of the Fe-Mn-Si Alloys in Physiological Solution*

The corrosion behavior of the three synthesized Fe-Mn-Si alloys is studied in Hank's solution at 310 K (37 °C) from the open circuit potential measurements in Figure 6.

Particularly, the comparison with pure iron and with the binary Fe-Mn alloy clearly indicates that the manganese as an alloying element increases the corrodibility (lowers the thermodynamic stability) of iron in the physiological solution. Additionally, silicon in ternary alloys causes a further decrease in the open circuit potential when compared to a binary alloy. Moreover, the measurements presented as a function of the manganese content point out that the corrodibility of the Fe-Mn-Si alloy in the physiological solution increases with its manganese content. The potential is shifted towards more negative values indicating an increase of the corrodibility of the alloy in terms of thermodynamics. Such a behavior is obviously attributed to the presence of manganese in the alloy that increases the electrochemical activity of the material. Indeed, manganese has a more negative standard potential than iron. Therefore, an increase of the manganese content in the alloy promotes electrochemical reactions in the physiological solution, *i.e.*, the corrosion of the material.[35,36]

Similar observations are highlighted from the polarization curves in Figure 7 that show the corrosion potential value of each sample under the same experimental conditions. Moreover, the corrosion behavior of the alloy is also assessed from a kinetics point of view by extracting the corresponding corrosion current density values ($i_{corr.}$) from these curves (Table II).

It is observable that the kinetics of the corrosion reactions is increased by the presence of manganese in the alloy particularly for the highest amounts. The addition of silicon causes an increase in the corrosion rate, possibly due to the formation of SiO_2 nonmetallic inclusions on the surface acting as cathodic sites facilitating the cathodic reaction that limits the overall corrosion process.

The corresponding corrosion rate (K_r) reported in Table II indicates fast degradability of these alloys in a physiological solution (about 1 mm/year).

The corrosion rate is also determined from the weight loss measurements conducted after the corrosion

Table II. Corrosion Potential ($E_{corr.}$), Corrosion Rate (K_r) Determined from Corrosion Current Density ($i_{corr.}$), and Corrosion Rate ($K_{\Delta m}$) Determined from Weight Loss Measurements

	E_{corr} (mV/SSCE)	i_{corr} (A/cm^2)	K_r (mm/year)	$K_{\Delta m}$ (mm/year)
Fe	− 571	$(1.0 \pm 0.3) \times 10^{-5}$	0.12 ± 0.04	0.10 ± 0.02
Fe30Mn	− 727	$(2.3 \pm 0.4) \times 10^{-5}$	0.26 ± 0.04	0.24 ± 0.03
Fe30Mn5Si	− 755	$(6.7 \pm 0.8) \times 10^{-5}$	0.80 ± 0.10	0.76 ± 0.08
Fe26Mn5Si	− 738	$(5.0 \pm 0.6) \times 10^{-5}$	0.59 ± 0.08	0.56 ± 0.06
Fe23Mn5Si	− 734	$(4.1 \pm 0.7) \times 10^{-5}$	0.48 ± 0.09	0.44 ± 0.05

experiments. The observed tendency is the same, indicating some close values. This result is interesting for biomedical applications since such material is typically expected to act during a short healing process.[16] For example, it could be used as a metallic stent to treat coronary artery diseases during few weeks or few months. Then, due to the action of the blood flow, the metallic stent is completely dissolved after the healing process, leaving no metallic material inside the body.[35,37] Moreover, in the case of a use to support a bone healing process, these biodegradable metallic alloys require only one surgical intervention and circumvent the need for the implant removal.[18] Therefore, they contribute to the patient comfort and help reduce medical costs. It is noticeable that the speed of the biodegradability process of the alloy can be adjusted by the manganese content introduced in the alloy and then producing a material able to degrade within a reasonable period. However, to further assess the degradation properties of these new implant materials, it will be necessary to conduct more extensive research using *in vitro* or *in vivo* tests during several weeks and several months in controlled environment, under mechanical stresses, and at a certain temperature with a monitored pH.[9]

IV. CONCLUSIONS

This work presents the synthesis and characterization of three Fe-(23-30)Mn-5Si (wt pct) alloys, the physicochemical and mechanical characteristics of which make them promising for biodegradable materials.

1. The phase composition and martensitic transformation features are modified as a function of the manganese content in the alloy. The M_s temperature of the γ-austenite $\rightarrow$ ε-martensite transformation decreases as the manganese content increases and approaches the body temperature at 30 wt pct Mn. This property provides conditions for the premartensitic lattice softening and related lowering of the Young's modulus, and indicates the way for shape memory realization at sufficiently low temperature, if required.
2. The Young's modulus of the studied alloys is twice lower than that of pure iron, particularly, for the highest manganese amount. This mechanical property together with sufficiently high yield stress makes these materials promising candidates for implant applications in terms of biomechanical compatibility and mechanical reliability.
3. The study of the biodegradation properties of the Fe-Mn-Si alloys, pure iron, and iron-manganese binary alloy in Hank's solution at 310 K (37 °C) shows that the corrosion rate of the Fe-Mn alloy is much higher than that of iron. The silicon addition to the binary alloy increases the corrosion rate.
4. The Fe30Mn5Si alloy shows the most promising properties for biomedical applications as a biodegradable implant material that combines high biodegradation rate with biomechanical compatibility and reliability during lifetime.

ACKNOWLEDGMENTS

The present work was carried out with the financial support of the Ministry of Education and Science of the Russian Federation, in the framework of the Increase Competitiveness Program of NUST "MISIS" (Grant No. K4-2016-57). The authors thank Dr. E. Bazanova, NUST "MISiS" Director of Academic Writing Office, for her critical reading of the manuscript and some helpful suggestions.

REFERENCES

1. Y.F. Zheng, X.N. Gu, and F. Witte: *Mater. Sci. Eng. R*, 2014, vol. 77, pp. 1–34.
2. H. Li, Y. Zheng, and L. Qin: *Prog. Nat. Sci.*, 2014, vol. 24, pp. 414–22.
3. M. Niinomi: *Metall. Mater. Trans. A*, 2002, vol. 33, pp. 477–86.
4. H. Hermawan, D. Dubé, and D. Mantovani: *Acta Biomater.*, 2010, vol. 6, pp. 1693–97.
5. M. Schinhammer, A.C. Hänzi, J.F. Löffler, and P.J. Uggowitzer: *Acta Biomater.*, 2010, vol. 6, pp. 1705–13.
6. A. Francis, Y. Yang, S. Virtanen, and A.R. Boccaccini: *J. Mater. Sci.*, 2015, vol. 26, pp. 138–53.
7. K. Otsuka and C.M. Wayman: *Shape Memory Materials*, Cambridge University Press, Cambridge, 1999.
8. V. Brailovski, S. Prokoshkin, P. Terriault, and F. Trochu: *Shape Memory Alloys: Fundamentals, Modelling and Applications*, ETS Publ, Montreal, 2003.
9. H. Hermawan, A. Purnama, D. Dube, J. Couet, and D. Mantovani: *Acta Biomater.*, 2010, vol. 6, pp. 1852–60.
10. Y.H. Wen, H.B. Peng, D. Raabe, I. Gutierrez-Urrutia, J. Chen, and Y.Y. Du: *Nat. Commun.*, 2014, vol. 5, p. 4964.
11. C.H. Yang, H.C. Lin, K.M. Lin, and H.K. Tsai: *Mater. Sci. Eng. A*, 2008, vol. 497, pp. 445–50.
12. T. Niendorf, F. Brenne, P. Hoyer, D. Schwarze, M. Schaper, R. Grothe, M. Wiesener, G. Grundmeier, and H.J. Maier: *Metall. Mater. Trans. A*, 2015, vol. 46, pp. 2829–33.
13. F. Witte: *Acta Biomater.*, 2010, vol. 6, pp. 1680–92.
14. A.H. Yusop, A.A. Bakir, N.A. Shaharom, M.R. Abdul Kadir, and H. Hermawan, *Int. J. Biomater.*, 2012, article number 641430.
15. J. Hufenbach, H. Wendrock, F. Kochta, U. Kühn, and A. Gebert: *Mater. Lett.*, 2017, vol. 186, pp. 330–33.
16. B. Liu, Y.F. Zheng, and Liquan. Ruan: *Mater. Lett.*, 2011, vol. 65, pp. 540–43.
17. M. Kaya and O. Cakmak: *Metall. Mater. Trans. A*, 2016, vol. 47, pp. 1499–1503.
18. T. Kraus, F. Moszner, S. Fischerauer, M. Fiedler, E. Martinelli, J. Eichler, F. Witte, E. Willbold, M. Schinhammer, M. Meischel, P.J. Uggowitzer, J.F. Löffler, and A. Weinberg: *Acta Biomater.*, 2014, vol. 10, pp. 3346–53.
19. F. Matassi, A. Botti, L. Sirleo, C. Carulli, and M. Innocenti: *Clin. Cases Miner. Bone Metab.*, 2013, vol. 10, pp. 111–15.
20. J. Wan and S. Chen: *Curr. Opin. Solid State Mater. Sci.*, 2005, vol. 9, pp. 303–12.
21. V.V. Bliznuk, V.G. Gavriljuk, B.D. Shanina, A.A. Konchits, and S.P. Kolesnik: *Acta Mater.*, 2003, vol. 51, pp. 6095–6103.
22. V. Brailovski, S. Prokoshkin, M. Gauthier, K. Inaekyan, S. Dubinskiy, M. Petrzhik, and M. Filonov: *Mater. Sci. Eng. C*, 2011, vol. 31, pp. 643–57.
23. H. Hermawan, M. Moravej, D. Dubé, M. Fiset, and D. Mantovani: *Adv. Mater. Res.*, 2007, vols. 15–17, pp. 113–18.
24. H. Hermawan, D. Dubé, and D. Mantovani: *J. Biomed. Mater. Res.*, 2010, vol. 93A, pp. 1–11.
25. V.G. Gavriljuk, V.V. Bliznuk, B.D. Shanina, and S.P. Kolesnik: *Mater. Sci. Eng. A*, 2005, vol. 406, pp. 1–10.
26. G. Wang, H. Peng, C. Zhang, S. Wang, and Y. Wen: *Smart Mater. Struct.*, 2016, vol. 25, p. 075013.
27. V. Fuster, A.V. Druker, A. Baruj, J. Malarría, and R. Bolmaro: *Mater. Charact.*, 2015, vol. 109, pp. 128–37.
28. D.M. Gordin, T. Gloriant, Gh. Nemtoi, R. Chelariu, N. Aelenei, A. Guillou, and D. Ansel: *Mater. Lett.*, 2005, vol. 59, pp. 2936–41.

29. M.I.Z. Ridzwan, S. Solehuddin, A.Y. Hassan, A.A. Shokri, and M.N. Ibrahim: *J. Med. Sci.*, 2007, vol. 7, pp. 460–67.
30. D.T. Reilly and A.H. Burstein: *J. Biomech.*, 1975, vol. 8, pp. 393–405.
31. A. Druker, A. Baruj, and J. Malarría: *Mater. Charact.*, 2010, vol. 61, pp. 603–12.
32. M. Schinhammer, C.M. Pecnik, F. Rechberger, A.C. Hanzi, J.F. Loffler, and P.J. Uggowitzer: *Acta Mater.*, 2012, vol. 60, pp. 2746–56.
33. F. Moszner, A.S. Sologubenko, M. Schinhammer, C. Lerchbacher, A.C. Hanzi, H. Leitner, P.J. Uggowitzer, and J.F. Loffler: *Acta Mater.*, 2012, vol. 59, pp. 981–91.
34. B.C. Maji, M. Krishnan, M. Sujata, Gouthama, and R.K. Ray, *Metall. Mater. Tans. A*, 2013, vol. 44A, pp. 172–85.
35. J. Lévesque, H. Hermawan, D. Dubé, and D. Mantovani: *Acta Biomater.*, 2008, vol. 4, pp. 284–95.
36. S. Stanciu, A. Ursanu, L.C. Trinca, T.A. Elena, S. Carmen, C. Munteanu, N. Cimpoesu, D. Acatrinei, E.V. Sindilar, T. Stanciu, M. Fantanariu, and L. Topliceanu: *Environ. Eng. Manag. J.*, 2016, vol. 15 (5), pp. 973–80.
37. Y.P. Feng, A. Blanquer, J. Fornell, H. Zhang, P. Solsona, M.D. Baró, S. Suriñach, E. Ibáñez, E. García-Lecina, X. Wei, R. Li, L.L. Barrios, E. Pellicer, C. Nogués, and J. Sort: *J. Mater. Chem. B*, 2016, vol. 4, pp. 6402–12.